Soft Matter, DOI: 10.1039/D5SM00585J

Complex remodeling of biomembranes and vesicles by condensate droplets - ESI

Reinhard Lipowsky

Max Planck Institute of Colloids and Interfaces,
14424 Potsdam, Germany [1]

30 July 2025

Electronic Supplementary Information (ESI) with the following sections, figures, and tables:

[1] Email: lipowsky@mpikg.mpg.de; URL: https://www.mpikg.mpg.de/rl/

S1 Examples for segregative phase separation

This section provides several examples for the phase diagrams of aqueous two-phase systems in the absence of membranes: (i) aqueous PEG-dextran solutions; (ii) binary mixtures of water and solute molecules; (iii) phase diagram of PGL-1 protein as measured in vivo; (iv) aqueous solutions of the soybean protein glycinin and sodium chloride; as well as (v) aqueous solutions of the fused in sarcoma (FUS) protein and potassium chloride.

For the examples (i) and (ii), aqueous phase separation proceeds in a segregative manner whereas the examples (iv) and (v) undergo associative phase separation. As mentioned in the main text, segregative and associative phase separation are distinguished here by the number of critical demixing points at constant temperature. Thus, the segregative phase diagrams for (i) and (ii) have one such point whereas the associative phase diagrams for (iv) and (v) have two such points. For the PGL-1 protein, the phase diagram has been measured in vivo as a function of protein concentration and temperature, which can be mapped onto the phase diagram for a binary mixture of water and solute. However, it is possible that more than one critical point will be found when the PGL-1 phase diagram is determined at constant temperature as a function of protein and salt concentration.

Segregative phase separation in PEG-dextran solutions. One aqueous two-phase system that has been studied in some detail is provided by aqueous solutions of the two water-soluble polymers PEG and dextran. These solutions undergo segregative phase separation for relatively small weight fractions of the two polymers and represent the classic example for aqueous two-phase systems.[1] Such systems, which are also known as aqueous biphasic systems, have been used for a long time in biochemical analysis and biotechnology and are intimately related to water-in-water emulsions[1,2].

The phase separation of the PEG-dextran solution leads to a PEG-rich phase, denoted by α, and to a dextran-rich phase, denoted by β, which coexist over a wide range of polymer concentrations. The corresponding phase diagram is displayed in Fig. S1 as a function of the two weight fractions $w_{\rm d}$ and $w_{\rm p}$ of dextran and PEG.[3] When these two weight fractions belong to the two-phase coexistence region, the polymer solution undergoes phase separation into the PEG-rich α and the dextran-rich β phase.

The compositions of the two coexisting phases α and β correspond to the end points of the tie lines, as shown by green dashed lines in Fig. S1 . One end point of these tie lines is located at small weight fractions $w_{\rm d}$ of dextran, corresponding to the PEG-rich phase α, as displayed by the red downward-pointing triangles in Fig. S1 . The other end point of the tie lines is located at small weight fractions $w_{\rm p}$ of PEG, corresponding to the dextran-rich phase β and the blue upward-pointing triangles in Fig. S1 . In general, as we move along a certain tie line, we change the volume fractions of the two coexisting phases for fixed interfacial tension $\Sigma_{\alpha\beta}$ of the interface between the two phases.

For the PEG-dextran solution studied in ref. 3, the critical demixing point was located at $w_{\rm d} = 0.0451$ and $w_{\rm p} = 0.0361$ as indicated in Fig. S1 . In general, the precise values of these weight fractions for the critical point depend on the obtained sample of the synthetic polymers, reflecting the polydispersity of these polymers.

Segregative phase separation in binary mixtures. The presumably simplest example for segregative phase separation is provided by a binary liquid mixture as modelled by two types of beads: water (W) beads representing three water molecules and solute (S) beads representing solute molecules.[4] In this coarse-grained molecular model, the solubility ζ is provided by the force parameter ratio

$$\zeta \equiv \frac{(f_{\rm WW} + f_{\rm SS})/2}{f_{\rm WS}} = \frac{(f_{\rm WW} + f_{\rm SS})/2}{f_{\rm SW}} \tag{S1}$$

which involves the two force parameters $f_{\rm WW}$ and $f_{\rm SS}$ between a pair of water and a pair of solute beads as well as the force parameter $f_{\rm WS} = f_{\rm SW}$ for a water bead interacting with a solute bead. As we increase $f_{\rm WS}$, contacts between water and solute beads become energetically less favorable. These contacts can be avoided by the segregation of the two types of beads. As a consequence, decreasing the solubility ζ by increasing $f_{\rm WS}$ leads to phase separation into a solute-poor and a solute-rich phase as in Fig. S2 .

Figure S1 Phase diagram of aqueous two-phase systems formed by PEG and dextran at room temperature. Reused with permission from ref. 3, American Chemical Society, 2012. The coordinates of the two-dimensional phase diagram are provided by the weight fractions w_d and w_p of dextran and PEG. The binodal line (black and red data points) separates the one-phase region at low weight fractions from the two-phase region at higher weight fractions. The critical demixing point (CDP) is at $w_d = 0.0451$ and $w_p = 0.0361$. The green dashed lines represent tie lines in the two-phase region. For weight fractions within the two-phase region, the PEG-dextran solution undergoes phase separation into a PEG-rich phase α (red downward-pointing triangles) and a dextran-rich phase β (blue upward-pointing triangles).

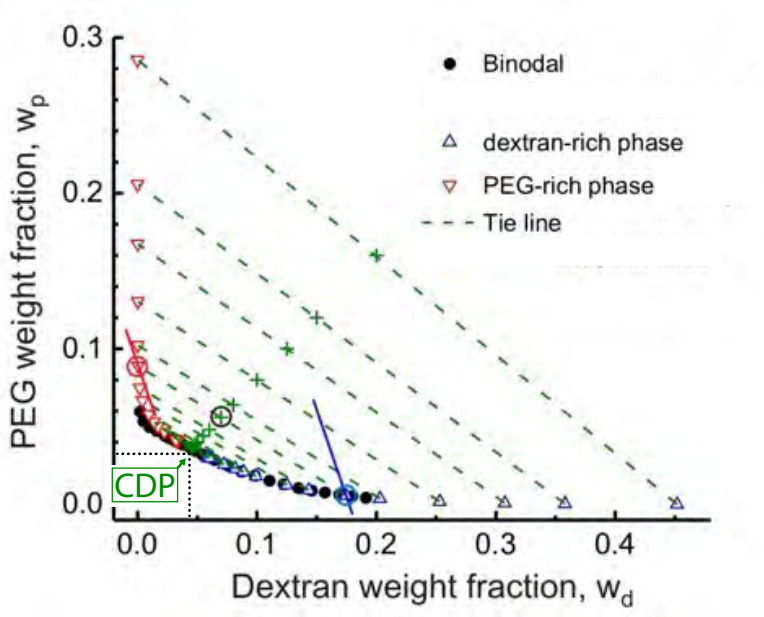

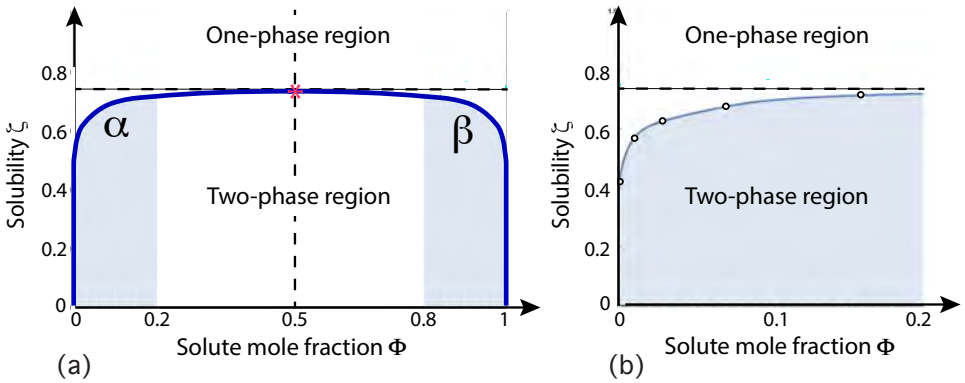

Figure S2 Phase diagram for a binary mixture of water and solute molecules as a function of solute mole fraction Φ_S and solubility ζ of the solute molecules in water[4]: (a) Global phase diagram for $0 \leq \Phi_S \leq 1$. The phase diagram is mirror symmetric with respect to the dashed vertical line at $\Phi_S = 1/2$, which implies horizontal tie lines. The critical demixing point (red star) with coordinates $(\Phi_S, \zeta) = (1/2, 0.746)$ is located at the crossing point of the dashed vertical line and the binodal line (dark blue); and (b) Phase diagram for $0 \leq \Phi_S \leq 0.2$ corresponding to the grey-shaded region on the left of (a). The four data points (open circles) on the binodal line have been determined by molecular dynamics simulations[4]. The binary mixture forms a uniform phase above the binodal line and undergoes phase separation into a water-rich phase α with $\Phi_S < 1/2$ and a solute-rich phase β with $\Phi_S > 1/2$ below the binodal line. Essentially the same phase diagram is obtained when solubility is replaced by temperature.

Segregative phase separation of PGL-1 protein condensates in vivo. Recently, condensate droplets enriched in certain proteins have also been observed within living cells. These protein condensates are believed to form via liquid-liquid phase separation in the cytoplasm and can be reconstituted in vitro, which makes it possible to measure the corresponding phase diagram. One example for such a phase diagram as determined in vivo is displayed in Fig. S3 .[5] Inspection of this figure shows that the phase diagram exhibits one critical point in close analogy to the phase of a binary liquid mixture as in Fig. S2 . As mentioned at the beginning of this section, it is, however, possible that more than one critical point will be found when the PGL-1 phase diagram

is determined at constant temperature as a function of protein and salt concentration.

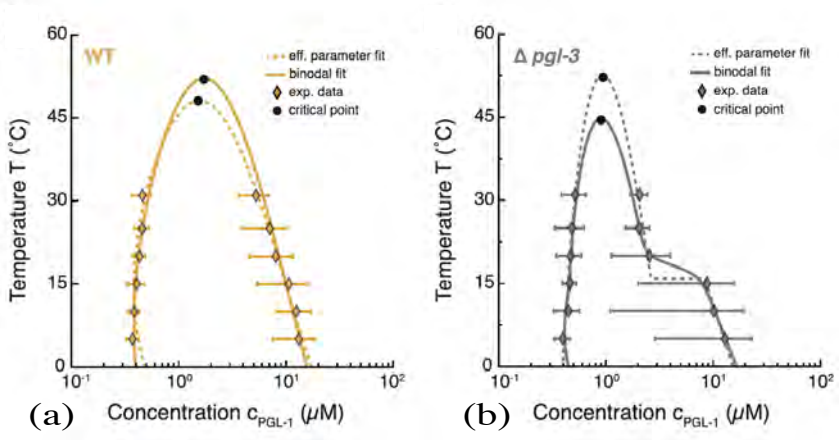

Figure S3 Phase diagram for condensates enriched in the protein PGL-1 as observed in P granules of *C. elegans* cells.[5] The two-dimensional phase diagrams are defined by the concentration c_{PGL-1} of the PGL-1 protein and by the temperature. The data in (a) were obtained for the wild type, those in (b) after the deletion of the protein PGL−3. The experimental data (diamonds) for the binodals are compared with theoretical binodals based on effective parameters for a binary liquid mixture, compare the phase diagram in Fig. S2 .

S2 Interfacial tension in aqueous PEG-dextran solutions

For aqueous two-phase systems formed by PEG-dextran solutions, the interfacial tension has been measured over the whole coexistence region within the phase diagram in Fig. S1 . The resulting data are displayed in Fig. S4 . Inspection of this figure shows that the observed interfacial tension $\Sigma_{\alpha\beta}$ varies over four orders of magnitude and is well-fitted by the power law $\Sigma_{\alpha\beta} \sim \Delta c^{\mu}$ with the critical exponent μ being close to its mean-field value[6] $\mu = 3/2$.

Figure S4 Interfacial tension $\Sigma_{\alpha\beta}$ of the liquid–liquid interface between the PEG-rich phase α and the dextran-rich phase β as a function of the polymer concentration $\Delta c \equiv (c - c_{cr})/c_{cr}$ where c_{cr} denotes the concentration at the critical demixing point. Reused with permission from ref. 3, American Chemical Society, 2012. The red data for the PEG-dextran solutions exhibit the power-law behavior $\Sigma_{\alpha\beta} \sim \Delta c^{\mu}$ where the critical exponent μ is close to its mean value[6] $\mu = 3/2$. For comparison, the dashed red line corresponds to $\mu = 1.26$ based on the hyperscaling relation[7] $\mu = 2\nu$ where ν is the critical exponent of the correlation length.

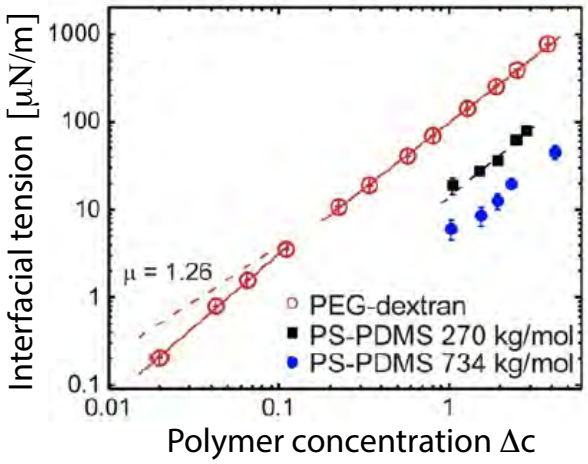

S3 Complete and partial wetting of giant vesicles in PEG-dextran solutions

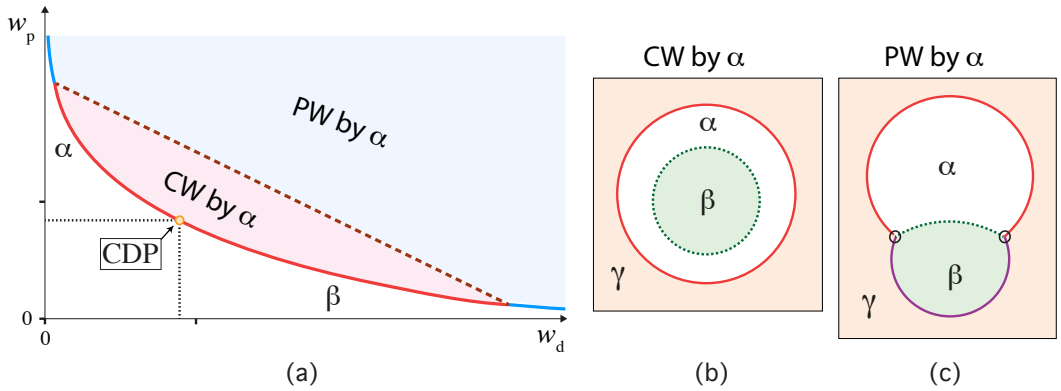

Figure S5 Schematic phase diagram and wetting regimes of aqueous PEG-dextran solutions within giant vesicles, with the PEG-rich phase α and the dextran-rich phase β: (a) Schematic phase diagram of PEG-dextran solutions at room temperature. The phase diagram exhibits (i) a one-phase region (white) at low weight fractions w_d and w_p of the dextran and PEG polymers as well as (ii) a two-phase region (light red and light blue) at higher weight fractions. The boundary between the one-phase and two-phase regions defines the binodal line which contains the critical demixing point (CDP, orange). The two-phase region above the binodal is divided up into two subregions, a complete wetting (CW) subregion (light red) close to the critical point and a partial wetting (PW) subregion (light blue), which are separated by a certain tie line (dashed purple line); (b) CW morphology and (c) PW morphology of the vesicle-droplet system corresponding to complete and partial wetting of the vesicle membrane by the PEG-rich α phase.

S4 Polymorphism of membrane nanotubes

Nanotubes and spontaneous curvature. When a vesicle forms membrane nanotubes in response to a reduction of its volume-to-area ratio $\bar{v}$, this tube formation provides direct evidence that the vesicle membrane has a relatively large spontaneous (or preferred) curvature.[8] Out-tubes pointing towards the exterior solution as in Fig. 7a have a large and positive mean curvature M_{tu}, caused by a large and positive value of the spontaneous curvature m with $M_{tu} \approx m \gg 1/R_{ve}$ where $R_{ve} = \sqrt{A/(4\pi)}$ is the vesicle size defined in terms of the membrane area A. On the other hand, in-tubes pointing towards the interior of a vesicle as in Fig. 7b have a large and negative mean curvature, generated by a large and negative spontaneous curvature with $M_{tu} \approx m \ll -1/R_{ve}$. Therefore, the formation of nanotubes requires a separation of length scales in the sense that the width of the tubes is small compared to the size of the vesicle.

In general, the formation of membrane nanotubes by the interaction with condensate droplets must as considered here must be distinguished from force-induced tubulation or tube pulling as obtained by the local application of external forces to the vesicle membranes.[9] In order to perform such tube pulling experiments, one must immobilize the vesicle and then apply a localized force which often acts on a membrane-bound bead. A particularly useful setup is obtained by micropipette aspiration of giant vesicles combined with an optical trap that pulls on the bead.[10–13].

Nanotubes for complete and partial wetting. For complete wetting of the vesicle membrane as in Fig. 7, each nanotube of an individual vesicle is confined to the complete wetting layer consisting of one of the coexisting liquid phases, α or β and, thus, enclosed by one type of membrane segment, $\alpha\gamma$ or $\beta\gamma$. As a consequence, for complete wetting, all nanotubes avoid the other liquid phase as well as the $\alpha\beta$ interface. In contrast, for partial wetting of the vesicle membrane by both coexisting liquid phases, the nanotubes adhere to the $\alpha\beta$ interface and then become divided up into an $\alpha\gamma$ and an $\beta\gamma$ segment as depicted in Fig. 9 and 24.

Different properties of out- and in-tubes. As mentioned before, out-tubes have a positive mean curvature whereas in-tubes have a negative mean curvature. In addition, the out- and in-tubes are connected to different volume reservoirs: the in-tubes exchange volume with the exterior aqueous solution, which represents an effectively unlimited volume reservoir, whereas the out-tubes exchange aqueous solution with the interior vesicle compartment. Furthermore, the membranes of out- and in-tubes experience different osmotic pressure differences: the membrane of an out-tube is subject to the same pressure difference, $\Delta P = P_{\rm in} - P_{\rm ex}$, as the membrane of the large spherical segment of the mother vesicle whereas an in-tube feels the opposite pressure difference equal to $-\Delta P = P_{\rm ex} - P_{\rm in}$.

Cylindrical shapes of nanotubes. In Fig. 7–9, the individual nanotubes were taken to have cylindrical shapes for visual simplicity. For the complete wetting geometry in Fig. 7, all cylindrical tubes of each vesicle are formed by the same membrane segment and have the same mean curvature $M_{\rm cy}$, which is equal to the spontaneous curvature $m_{\beta\gamma}$ of the $\beta\gamma$ segment in Fig. 7a and to the spontaneous curvature $m_{\alpha\gamma}$ of the $\alpha\gamma$ segment in Fig. 7b as follows from the quantitative analysis for the nanotubes protruding from a uniform vesicle membrane.[8] Therefore, all cylindrical out-tubes in Fig. 7a have the radius $R_{\rm cy} = 1/(2m_{\beta\gamma})$, and all cylindrical in-tubes in Fig. 7b have the radius $R_{\rm cy} = 1/(2|m_{\alpha\gamma}|)$.

Different shapes of freely suspended nanotubes. For complete wetting of the vesicle membrane, the membrane forms nanotubes that are completely immersed in one of the two coexisting liquid phases as in Fig. 7. These nanotubes can attain a variety of different shapes, corresponding to cylinders, unduloids, and multispherical tubes, all of which represent Delaunay surfaces.[14] Two of these Delaunay surface shapes, cylinders and multispherical tubes, are depicted in Fig. S6 . The multispherical tube is closed on itself whereas the cylindrical tube has been supplemented by a spherical endcap. Apart from this endcap, all Delaunay shapes have a constant mean curvature and fulfill the local shape equation of curvature elasticity for mean curvature $M = m$.[15] In addition, in the absence of shape fluctuations, all of these shapes have zero bending energy which implies that they can be easily transformed into one another.[16]

Indeed, multispherical tubes as in Fig. S6 a can be transformed into cylindrical shapes as in Fig. S6 b via intermediate unduloids. This transformation proceeds in a continuous manner without being hindered by an energy barrier. Close to the multispherical tube shape, the intermediate unduloids exhibit open necks with small neck radii whereas the necks and bellies of the intermediate unduloids approach the same radii close to the cylindrical tube shape.

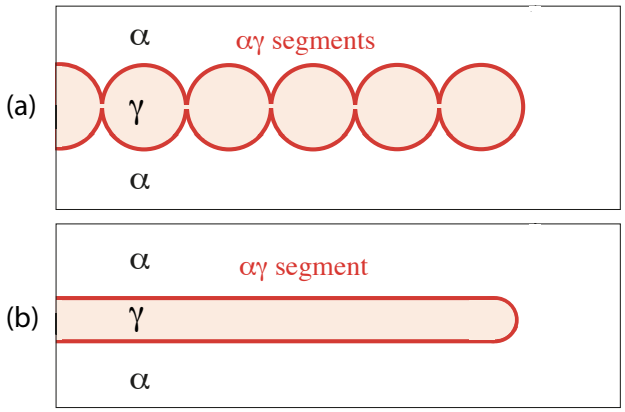

Figure S6 Different shapes of membrane nanotubes (red) for complete wetting. The nanotubes are freely suspended in the α phase (white) and filled with γ phase (pink), : (a) Multispherical tube consisting of equally sized spheres that are connected by closed membrane necks; and (b) Cylindrical shape closed with a spherical endcap. Apart from the spherical endcaps, the tubes in (a) and (b) have the same mean curvature M, which is equal to the spontaneous curvature m. The radius of the spheres in (a) is twice as large as the radius of the cylinder.

Different shapes of adhering nanotubes. For partial wetting of the vesicle membrane by the two coexisting liquid phases α and β, the nanotubes adhere to the $\alpha\beta$ interface as in Fig. 9 and 24. The shape of such an adhering nanotube is determined by the interplay between bending and adhesion. Furthermore, the adhering nanotubes are divided up into two distinct membrane segments, the $\alpha\gamma$ segment in contact with the α phase and the $\beta\gamma$ segment exposed to the β phase, as indicated by the different colors (red and purple) in Fig. 9 and 24. These two segments will, in general, have different curvature-elastic properties and, in particular, different spontaneous curvatures $m_{\alpha\gamma}$ and $m_{\beta\gamma} \neq m_{\alpha\gamma}$. As a consequence, the mean curvatures $M_{\alpha\gamma}$ and $M_{\beta\gamma}$ of the $\alpha\gamma$ and

$\beta\gamma$ tube segments exhibit a curvature discontinuity as in eqn (3). The precise shapes of such nanotubes remain to be calculated in a systematic manner but the angle between the $\alpha\gamma$ membrane segment and the $\alpha\beta$ interface must be equal to the intrinsic contact angle θ_α^* as in Fig. 24.

Transition from multispherical to cylindrical tubes. Inward-pointing nanotubes are predicted to undergo a transition from multispherical to cylindrical shapes at a certain threshold value, $L_{\rm cy}^*$, of the tube length $L_{\rm cy}$: short tubes with $L_{\rm cy} < L_{\rm cy}^*$ should have a multispherical shape whereas long tubes with $L_{\rm cy} > L_{\rm cy}^*$ should have a cylindrical shape.[17] Experimental evidence for this shape transformation from multispherical to cylindrical tubes has been obtained for nanotubes adhering to the $\alpha\beta$ interface inside giant vesicles as in Fig. 9b and 10b. More precisely, confocal microscopy revealed the coexistence of both short multispherical and long cylindical tubes formed by the same vesicle membrane as shown in Fig. S7 b.

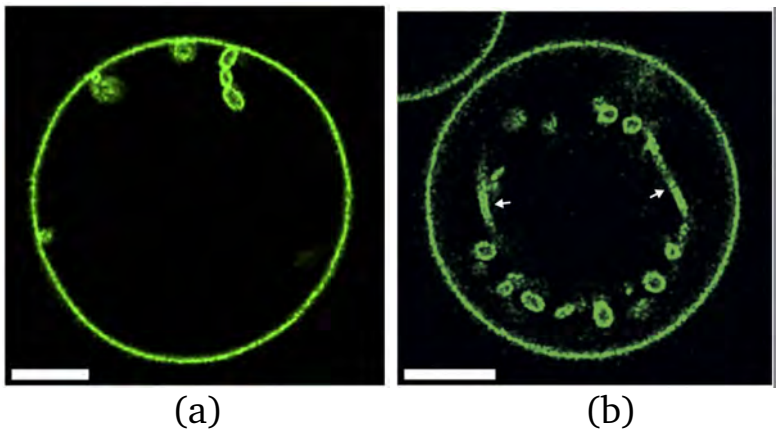

Figure S7 Giant vesicle membranes in the liquid-ordered phase (green), forming in-tubes that point towards the vesicle interior: (a) Several buds and one multispherical or necklace-like tube consisting of three deformed spheres; and (b) Several multispherical tubes and two cylindrical tube segments (white arrows) formed by the $\alpha\gamma$ membrane segment of the vesicle membrand and adhering to the $\alpha\gamma$ interface.[17]

S5 Spontaneous curvature and curvature-elastic tension

The spontaneous curvature m of vesicle membranes can vary over a wide range as in the first row of Table S1, where we provide the m-values as obtained from several experimental studies of giant vesicles.[17–19] In the case of His-tagged GFP, it was possible to directly control the spontaneous curvature by the nanomolar concentration of this protein in the exterior solution and by the small mole fraction of anchor lipids in the membrane.[19] The curvature-elastic tension $\sigma = 2\kappa m^2$, as given in the third row of Table S1, is then obtained from the m-values in the first row of this table, supplemented by measurements or estimates of the bending rigidity κ.[17–19]

Lipids	POPC:Chol	DOPC:DPPC:Chol	DOPC:DPPC:Chol	POPC:POPG:Chol
Lipid comp	90:10	13:44:43, Lo phase	64:15:21, Ld phase	70:10:20
Solutes	glucose, sucrose[18]	PEG, dextran[17]	PEG, dextran[17]	His-tagged GFP[19]
m [1/μm]	1.3	-1.6	-8	1.45 – 29
κ [10^{-19} J]	$\simeq 1$	3.6	0.8	2
σ [mN/m]	3.4×10^{-4}	2.1×10^{-3}	10^{-2}	0.8×10^{-4} – 3.4×10^{-1}

Table S1 Spontaneous curvature m, bending rigidity κ, and curvature-elastic tension $\sigma = 2\kappa m^2$ for four different lipid-solute systems corresponding to the four columns of the table. In each system, the lipids are assembled into bilayers of giant vesicles, which are exposed to different solute concentrations in the interior and exterior solutions. The first column provides the results for the binary lipid mixture of POPC and 10 mol% cholesterol[18]; the second and third column for a ternary lipid mixture in the liquid-ordered (Lo) and liquid-disordered (Lo) phase;[17] the fourth column for a ternary lipid mixture doped with anchor lipids that bind the His-tagged GFP molecules[19]. For the bending rigidity κ of the POPC:Chol bilayers, different values in the range from 0.8 to 2.2 $\times10^{-19}$ J have been reported[21–24] and are replaced here by the conservative estimate $\kappa \simeq 10^{-19}$ J. The bending rigidities in the second and third column are taken from ref. 20.

S6 Line tension of contact lines between membranes and droplets

Positive and negative contact line tensions. The contribution of the contact line to the free energy of the vesicle-droplet system is proportional to the line tension $\lambda_{\rm cl}$ of the contact line. A positive line tension favors a circular contact line whereas a negative line tension favors a strongly non-circular or tight-lipped shape of contact line as in Fig. 13. A negative line tension implies that the contact line would like to increase its length $L_{\rm cl}$. At the same time, the system would also like to reduce the area of the $\alpha\beta$ interface, which is bounded by the contact line. Thus, for a negtive contact line tension, the vesicle-droplet system tries to maximize the length of the contact line and to simultaneously minimize the area of the $\alpha\beta$ interface.

For liquid mixtures without membranes, the notion of line tension was already introduced by Gibbs who called it "linear tension" and pointed out that this tension may be positive or negative.[30,31] In contrast, interfacial tensions must always be positive as required by the thermodynamic stability of the interfaces. In the absence of membranes, negative values of the line tension have been observed for sessile liquid droplets on solid surfaces[32], for lense-shaped droplets between two bulk liquids[33], and in simulations of Lennard-Jones fluids[34]. Negative line tensions have also been found for Plateau borders in foams.[35]

Simulation results for contact line tensions. The mechanical tensions $\Sigma^{\rm m}_{\alpha\gamma}$ and $\Sigma^{\rm m}_{\beta\gamma}$ of the two membrane segments $\alpha\gamma$ and $\beta\gamma$ are essential in order to classify the wetting geometries in terms of contact angles and to define the affinity contrast, which provides a global view of the possible wetting transitions as in Fig. 19. In order to further elucidate the two pathways for complete engulfment and endocytosis of droplets, as depicted in Fig. 12 and 13, we have to consider the individual leaflets of the bilayer membranes and decompose the bilayer tension Σ according to[36–40]

$$\Sigma = \Sigma_{l1} + \Sigma_{l2} \tag{S2}$$

where Σ_{l1} and Σ_{l2} represent the two leaflet tensions. In the simulations, these leaflet tensions can be controlled by the lipid numbers that are assembled into the leaflets.

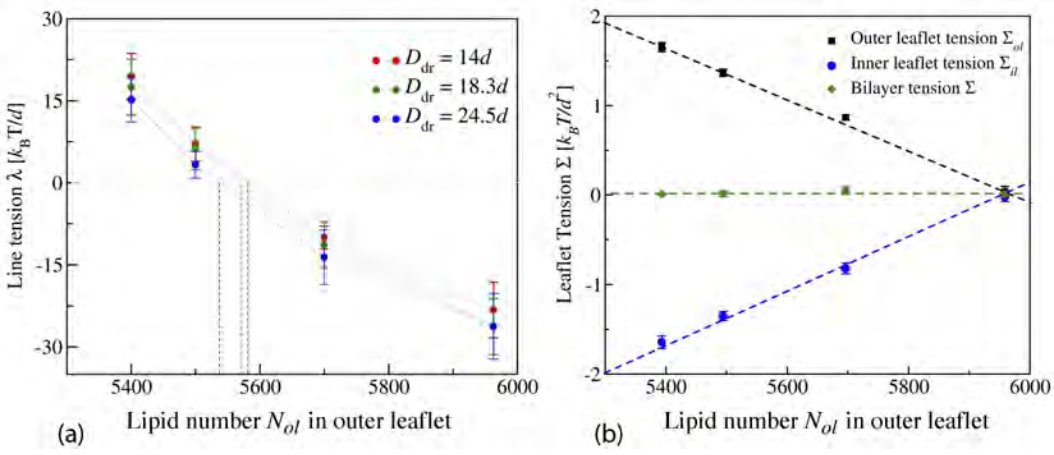

Figure S8 (a) Contact line tension $\lambda = \lambda_{\rm cl}$ as a function of lipid number N_{ol} in the outer leaflet, for three different droplet diameters $D_{\rm dr}$; and (b) Leaflet tensions Σ_{il} and Σ_{ol} in the inner and outer leaflet versus N_{ol}, corresponding to the blue and black data points. The bilayer tension $\Sigma = \Sigma_{il} + \Sigma_{ol}$ is close to zero (green data points).[39]

It is important to realize that the two leaflets of a tensionless bilayer with $\Sigma = 0$ can still experience significant leaflet tensions. Indeed, because $\Sigma = \Sigma_{l1} + \Sigma_{l2}$, the leaflet tensions of a tensionless bilayer with $\Sigma = 0$ satisfy $\Sigma_{l2} = -\Sigma_{l1}$, corresponding to one stretched and one compressed leaflet. Furthermore, each tensionless bilayer can be characterized by its stress asymmetry

$$\Delta\Sigma = \Sigma_{l1} - \Sigma_{l2} = 2\Sigma_{l1} = -2\Sigma_{l2}\,. \tag{S3}$$

The stress asymmetry $\Delta\Sigma$ is positive if leaflet l_1 is stretched with $\Sigma_{l1} > 0$ and leaflet l_2 is compressed with $\Sigma_{l2} < 0$ whereas $\Delta\Sigma$ is negative if l_1 is compressed and l_2 is stretched. Furthermore, vanishing stress asymmetry of a tensionless bilayer implies that both leaflet tensions are equal to zero, which defines the unique reference state of the bilayer.

Tight-Lipped Membrane Necks for Small Stress Asymmetries. For small stress asymmetries between the two leaflet tensions of a nanovesicle, complete engulfment leads to a tight-lipped membrane neck as displayed in Fig. 13. In this example, the outer leaflet of the vesicle is assembled from $N_{ol} = 5700$ lipids, the inner leaflet from $N_{il} = 4400$ lipids. When the bilayer tension $\Sigma = \Sigma_{ol} + \Sigma_{il}$ of this nanovesicle is close to zero, the vesicle has the initial stress asymmetry $\Delta\Sigma = \Sigma_{ol} - \Sigma_{il} \simeq 1.7\, k_B T/d^2$ between the leaflet tensions Σ_{ol} and Σ_{il} of the outer and inner leaflet where $d \simeq 0.8\,\text{nm}$ is the bead diameter of the coarse-grained molecular model studied in the simulations.

The positive value of the initial stress asymmetry $\Delta\Sigma$ implies that the outer leaflet is stretched whereas the inner leaflet is compressed. In order to reduce this stress asymmetry, the bilayer prefers to bulge towards the inner leaflet, thereby increasing the area of the inner leaflet and decreasing the area of the outer one. When a β droplet with a diameter of $14\,d$ or $11.2\,\text{nm}$ adheres to this vesicle, the contact line between droplet and vesicle has the *negative* line tension $\lambda_{\text{cl}} \simeq -10\, k_B T/d$, see Fig. S8 a, which leads to a tight-lipped membrane neck for the completely engulfed droplet as observed in the simulations.[39]

Axisymmetric Necks and Endocytosis for Large Stress Asymmetries. For sufficiently large stress asymmetries $\Delta\Sigma = \Sigma_{ol} - \Sigma_{il} > 0$, the line tension λ_{cl} of the contact line acquires a positive value.[39] One example is provided by a nanovesicle with $N_{ol} = 5500$ lipids in its outer leaflet and $N_{il} = 4600$ lipids in its inner leaflet as in Fig. 12. When the bilayer tension of the latter nanovesicle is close to zero, the vesicle has the initial stress asymmetry $\Delta\Sigma \simeq 2.7\, k_B T/d^2$. Adhesion of a droplet with a diameter of $11.2\,\text{nm}$ then leads to a contact line with *positive* line tension $\lambda_{\text{cl}} \simeq +7 k_B T/d$ and to a membrane neck that closes in an axisymmetric manner during complete engulfment, as shown in the first two snapshots of Fig. 12. After the neck has been closed, it undergoes fission, thereby generating two nested daughter vesicles as in the last snapshot of Fig. 12.

The transbilayer stress asymmetry plays the same role for nanovesicles as the spontaneous curvature for giant vesicles. In the latter case, the theory of curvature elasticity predicts that a sufficiently large spontaneous curvature generates a strong constriction force at the membrane neck that is sufficient to cleave the neck[41] as has been observed experimentally for giant unilamellar vesicles[19]. The endocytic process in Fig. 12 demonstrates an analogous fission mechanism for nanovesicles, with neck cleavage and vesicle division being induced by a sufficiently large transbilayer stress asymmetry $\Delta\Sigma = \Sigma_{ol} - \Sigma_{il} > 0$.

Competition between interfacial tension and line tension. The free energy contribution E_{cl} arising from the contact line is given by $E_{\text{cl}} = \lambda_{\text{cl}} L_{\text{cl}}$, where L_{cl} denotes the length of the contact line. The free energy contribution $E_{\alpha\beta}$ arising from the $\alpha\beta$ interface is equal to $E_{\alpha\beta} = \Sigma_{\alpha\beta} A_{\alpha\beta}$ where $A_{\alpha\beta}$ is the area of the $\alpha\beta$ interface. If the length L_{cl} of the contact line is comparable to the linear dimensions of the $\alpha\beta$ interface and, thus, to $\sqrt{A_{\alpha\beta}}$, the ratio of the line free energy to the interfacial free energy is given by

$$\frac{E_{\text{cl}}}{E_{\alpha\beta}} \sim \frac{\lambda_{\text{cl}} \sqrt{A_{\alpha\beta}}}{\Sigma_{\alpha\beta} A_{\alpha\beta}} = \frac{\lambda_{\text{cl}}}{\Sigma_{\alpha\beta} \sqrt{A_{\alpha\beta}}} \sim \frac{\lambda_{\text{cl}}}{\Sigma_{\alpha\beta} L_{\text{cl}}} \tag{S4}$$

which decays as $1/\sqrt{A_{\alpha\beta}} \sim 1/L_{\text{cl}}$ for large interfacial area $A_{\alpha\beta} \sim L_{\text{cl}}^2$. More precisely, the line tension contribution to the free energy becomes negligible when the contact line length L_{cl} is large compared to $|\lambda_{\text{cl}}|/\Sigma_{\alpha\beta}$, where the absolute value of λ_{cl} takes into account that the contact line tension can be positive or negative. On the other hand, the line tension contribution becomes significant when the contact line length L_{cl} satisfies

$$L_{\text{cl}} \lesssim |\lambda_{\text{cl}}|/\Sigma_{\alpha\beta}\,. \tag{S5}$$

Force balance relation with contact line tension. The line tension of the contact line contributes the additional free energy term $E_{\text{cl}} = \lambda_{\text{cl}} L_{\text{cl}}$ to the vesicle-droplet system. When we include this term in the shape functional, minimization of this functional leads to a force balance relation between the three surface tensions and the contact line tension λ_{cl}. For axisymmetric shapes, the contact line tension λ_{cl} is positive as shown in Fig S8 . The tangential (or parallel) force balance is then given by[29,42]

$$\Sigma_{\beta\gamma}^{\text{m}} - \Sigma_{\alpha\gamma}^{\text{m}} = \Sigma_{\alpha\beta} \cos\theta_{\alpha}^{*} + \frac{\lambda_{\text{cl}}}{R_{\text{cl}}} \cos\psi_{\text{cl}} \tag{S6}$$

which is equivalent to the rescaled affinity contract

$$w_{\beta\alpha} = \frac{\Sigma^{\rm m}_{\beta\gamma} - \Sigma^{\rm m}_{\alpha\gamma}}{\Sigma_{\alpha\beta}} = \cos\theta^*_\alpha + \frac{\lambda_{\rm cl}}{\Sigma_{\alpha\beta} R_{\rm cl}} \cos\psi(s_{\rm cl})\,. \tag{S7}$$

The last term on the right hand side of this equation is proportional to $\lambda_{\rm cl}/(\Sigma_{\alpha\beta}R_{\rm cl})$. This additional term becomes significant for sufficiently short contact lines, for which the contact line radius $R_{\rm cl}$ satisfies

$$R_{\rm cl} \lesssim \frac{|\lambda_{\rm cl}|}{\Sigma_{\alpha\beta}}\,. \tag{S8}$$

in accordance with eqn (S5). The condition as given by eqn (S8) is eventually fulfilled when the membrane neck adjacent to the contact line becomes closed during the complete engulfment of the condensate droplet as displayed in Fig. 5 and 6. As a consequence, the positive or negative sign of the line tension strongly affects the closure of the membrane neck as described in Section 9 of the main text.

S7 Formation of nanotubes after complete engulfment of condensate droplets

As explained in Sections 4–6 and 8, reducing the volume-to-area ratio $\bar{v}$ of giant vesicles by decreasing their volume or by increasing their membrane area can lead to the complete engulfment of condensate droplets or, alternatively, to the formation of membrane nanotubes. Complete engulfment is obtained for large interfacial tensions $\Sigma_{\alpha\beta}$ that satisfy eqn (12). What happens when we continue to deflate the vesicle after the condensate droplet has been completely engulfed? If the membrane segment $\alpha\gamma$ has a sufficiently large curvature-elastic tension $\sigma_{\alpha\gamma}$, this segment will then form nanotubes in order to store the additional excess area released by the deflation. The resulting coexistence of completely engulfed condensate droplets and nanotubes has been recently observed for exterior glycinin-rich droplets at vesicle membranes with azo-PC lipids that undergo conformotional transitions upon illumination, see Fig. S9 .[43]

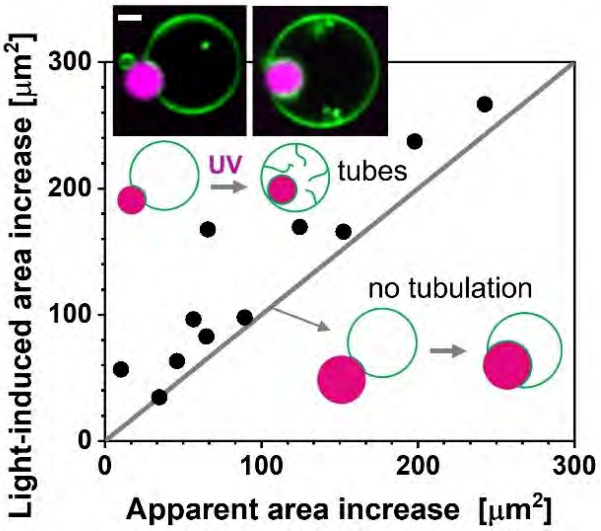

Figure S9 Vesicle membranes containing azo-lipids, which undergo conformational transitions when illuminated by UV and blue light, thereby changing the membrane area of the vesicle. UV light leads to a transition from the *trans*- to the *cis*-conformations of the azo-lipids, which increases the membrane area. Blue light leads back from *cis* to *trans*, which decreases the membrane area. In the figure, area increase induced by UV light is plotted agains increase of apparent membrane area. When the light-induced area exceeds the apparent area increase, the $\alpha\gamma$ membrane segments (green) form in-ward pointing nanotubes.[43]

S8 Morphological pathways for the axisymmetric closure of membrane necks

S8.1 Parametrization of axisymmetric two-droplet vesicles

Consider an axisymmetric vesicles enclosing an α and β droplet, which are separated by an $\alpha\beta$ interface. The corresponding shape contour is displayed in Fig. S10 . The contour is parametrized by arc length s with

$s = s_{\rm npol} = 0$ at the north pole and $s = s_{\rm spol}$ at the south pole. The circular contact line is located at $s = s_{\rm cl}$, the circular membrane neck at $s = s_{\rm ne}$.

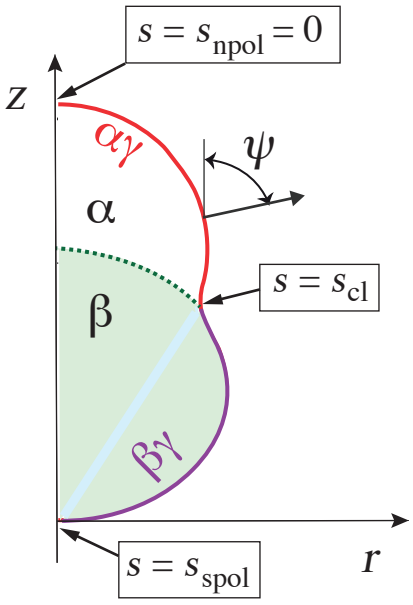

Figure S10 Axisymmetric shape corresponding to partial wetting of the vesicle membrane (red/purple) enclosing two interior droplets of α phase (white) and β phase (green). The two droplets are separated by an $\alpha\beta$ interface (dotted green). The two-dimensional membrane shape is uniquely determined by the one-dimensional shape contour (red-purple) in the (r,z)-plane defined by the coordinate z parallel to the axis of rotational symmetry and the radial coordinate r, which measures the distance from this symmetry axis. The shape contour is parametrized by arc length s, with the north and south pole of the vesicle being located at $s = s_{\rm npol} = 0$ and $s = s_{\rm spol}$. The circular contact line is located at $s = s_{\rm cl}$. The angle $\psi = \psi(s)$ describes the tilt angle of the membrane's normal vector from the vertical z-axis.

S8.2 Curvature discontinuities at the contact line

Consider any circle of latitude on the vesicle membrane, which is axisymmetric with respect to the z-axis in Fig. S10. We denote the principal curvature perpendicular to such a circle by $C_\perp$ and the principal curvature parallel to such a circle by $C_\parallel$. The principal curvature $C_\perp$ is equal to the curvature of the shape contour. In terms of the tilt angle ψ and the radial coordinate r, the principal curvatures $C_\perp$ and $C_\parallel$ are given by

$$C_\perp = \frac{\partial \psi}{\partial s} \quad \text{and} \quad C_\parallel = \frac{\sin\psi}{r}. \tag{S9}$$

The contour curvature $C_\perp$ can be discontinuous at the contact line whereas the parallel principal curvature $C_\parallel$ is always continuous across this line.[25] The discontinuous behavior of $C_\perp$ leads to a discontinuous behavior of the mean curvature $M = \frac{1}{2}(C_\perp + C_\parallel)$ as given by eqn (11) in the main text. Because of the continuity of the tilt angle ψ at the contact line, the contours of the $\alpha\gamma$ and $\beta\gamma$ membrane segments meet with a common tangent at the contact line but both the contour curvature $C_\perp(s) = \partial\psi/\partial s$ and the mean curvature $M(s)$ will, in general, exhibit a jump at $s = s_{\rm cl}$.

S8.3 Closure of contact line necks

The vesicle membrane in Fig. S10 exhibits an open neck at arc length $s = s_{\rm ne}$. The position of the neck is defined by its waistline with

$$\psi(s_{\rm ne}) = \frac{\pi}{2} \quad , \quad \left.\frac{\partial r}{\partial s}\right|_{r=r(s_{\rm ne})} = 0 \quad , \quad \text{and} \quad \left.\frac{\partial^2 r}{\partial s^2}\right|_{r=r(s_{\rm ne})} > 0, \tag{S10}$$

that is, by a normal vector with tilt angle $\psi = \psi(s_{\rm ne}) = \pi/2$ perpendicular to the z-axis of rotational symmetry and by a local minimum of the radial coordinate $r = r(s)$. The radius $R_{\rm ne}$ of the open neck is equal to $r(s_{\rm ne})$.

In the main text, a contact line neck has been defined by contact line radius $R_{\rm cl} = R_{\rm ne}$, that is, by the contact line being located at the waistline of the membrane neck during neck closure. In fact, all conclusions about the different morphological pathways as discussed in the main text remain valid if we use the more general property

$$R_{\rm cl} \approx \rho R_{\rm ne} \quad \text{for small neck radius } R_{\rm ne} \text{ with a dimensionless coefficient } \rho \text{ of order one} \tag{S11}$$

to define a contact line neck. In the following subsections, we use $\rho = 1$ for notational simplicity.

S8.4 Geometry of endocytic and exocytic two-sphere shapes

Endocytic and exocytic engulfment of the condensate droplets lead to an in-budded and out-budded vesicle-droplet morphology. When the radius $R_{\rm cl}$ of the circular contact line satisfies $R_{\rm cl} = R_{\rm ne}$ during neck closure, the two-droplet vesicle becomes a two-sphere vesicle in the limit of $R_{\rm ne} = R_{\rm cl} = 0$, corresponding to a closed contact line neck as shown in panels (a) and (b) of Fig. 5. In this limit, the spherical $\alpha\gamma$ and $\beta\gamma$ membrane segments can be characterized by their curvature radii $R_{\alpha\gamma}$ and $R_{\beta\gamma}$. These curvature radii are determined by the droplet volumes V_β and V_γ via

$$R_{\alpha\gamma} = \left(\frac{3}{4\pi}\right)^{1/3} \left(V_\beta + V_\gamma\right)^{1/3} \quad \text{and} \quad R_{\beta\gamma} = \left(\frac{3}{4\pi}\right)^{1/3} V_\beta^{1/3} \quad \text{for endocytic two-sphere shapes} \tag{S12}$$

and by the droplet volumes V_α and V_β according to

$$R_{\alpha\gamma} = \left(\frac{3}{4\pi}\right)^{1/3} V_\alpha^{1/3} \quad \text{and} \quad R_{\beta\gamma} = \left(\frac{3}{4\pi}\right)^{1/3} V_\beta^{1/3} \quad \text{for exocytic two-sphere shapes.} \tag{S13}$$

In both examples depicted in Fig. 5, the curvature radius $R_{\alpha\gamma}$ of the spherical $\alpha\gamma$ segment is taken to be larger than the curvature radius $R_{\beta\gamma}$ of the spherical $\beta\gamma$ segment.

S8.5 Curvature energy of two-sphere shapes

For both endocytic and exocytic two-sphere shapes, the bending energy of the vesicle membrane depends on the curvature-elastic parameters of the two membrane segments $\alpha\gamma$ and $\beta\gamma$. As in Section 7 of the main text, we denote the bending rigidity of the $\alpha\gamma$ membrane segment by $\kappa_{\alpha\gamma}$, its spontaneous curvature by $m_{\alpha\gamma}$, and its Gaussian curvature modulus by $\kappa_{G,\alpha\gamma}$. Likewise, the $\beta\gamma$ segment has bending rigidity $\kappa_{\beta\gamma}$, spontaneous curvature $m_{\beta\gamma}$, and Gaussian curvature modulus $\kappa_{G,\beta\gamma}$. The membrane of the two-sphere vesicle consists of a spherical $\alpha\gamma$ segment with radius $R_{\alpha\gamma}$ and a spherical $\beta\gamma$ segment with radius $R_{\beta\gamma}$. The bending energy of such a two-sphere vesicle is given by

$$E_{\rm be}(R_{\rm ne} = 0) = 8\pi\kappa_{\alpha\gamma}(1 - R_{\alpha\gamma}m_{\alpha\gamma})^2 + 8\pi\kappa_{\beta\gamma}(1 - R_{\beta\gamma}m_{\beta\gamma})^2 \quad \text{for exocytic two-sphere shapes} \tag{S14}$$

as in Fig. 5b and by

$$E_{\rm be}(R_{\rm ne} = 0) = 8\pi\kappa_{\alpha\gamma}(1 - R_{\alpha\gamma}m_{\alpha\gamma})^2 + 8\pi\kappa_{\beta\gamma}(1 + R_{\beta\gamma}m_{\beta\gamma})^2 \quad \text{for endocytic two-sphere shapes} \tag{S15}$$

as in Fig. 5a with $R_{\alpha\gamma} > R_{\beta\gamma}$. For endoctic two-sphere shapes with $R_{\beta\gamma} > R_{\alpha\gamma}$, the bending energy is obtained from eqn (S15) by swapping the $\alpha\gamma$ and $\beta\gamma$ subscripts.

A second contribution to the curvature energy of the two-sphere vesicle is given by the shape-dependent part of the Gaussian curvature energy, which is equal to

$$\Delta E_G = 2\pi(\kappa_{G,\beta\gamma} - \kappa_{G,\alpha\gamma})\cos\psi(s_{\rm cl})\,. \tag{S16}$$

For a contact line neck with $\psi(s_{\rm cl}) = \psi(s_{\rm ne}) = \pi/2$, this contribution of the Gaussian curvature energy vanishes. Therefore, for a closed contact line neck, the two-droplet vesicle becomes a two-sphere vesicle with the total energy

$$E_{\rm 2Sph} = E_{\rm be}(R_{\rm ne} = 0) \quad \text{(for a contact line neck with } R_{\rm ne} = R_{\rm db} = 0\text{)}. \tag{S17}$$

which depends on the bending energy $E_{\rm be}(R_{\rm ne} = 0)$ as given by eqn (S14) for the exocytic and by eqn (S15) for the endocytic case with $R_{\alpha\gamma} > R_{\beta\gamma}$.

S8.6 Two-droplet vesicle with small but finite radius of membrane neck

For small but finite values of the neck radius R_{ne}, the bending energy of a contact line neck has the asymptotic behavior

$$E_{\mathrm{be}}(R_{\mathrm{ne}}) \approx E_{\mathrm{2Sph}} + \zeta_{\mathrm{be}} R_{\mathrm{ne}} \quad \text{with} \quad \zeta_{\mathrm{be}} \equiv \left.\frac{\partial E_{\mathrm{be}}}{\partial R_{\mathrm{ne}}}\right|_{R_{\mathrm{ne}}=R_{\mathrm{cl}}=0} \quad \text{for small } R_{\mathrm{ne}}. \tag{S18}$$

The coefficient ζ_{be} of the term proportional to R_{ne} can be computed from the piecewise-constant-mean-curvature (P-CMC) parametrization of the vesicle shape, consisting of two hemispheres and two unduloid segments, as previously used for domain boundary necks.[26,28] The coefficient ζ_{be} obtained in this manner is given by

$$\zeta_{\mathrm{be}} = \zeta_{\mathrm{be}}^{\mathrm{exo}} \equiv 4\pi \left[\kappa_{\alpha\gamma}(m_{\alpha\gamma} - M_{\alpha\gamma}) + \kappa_{\beta\gamma}(m_{\beta\gamma} - M_{\beta\gamma})\right] = 4\pi \left[\kappa_{\alpha\gamma}\left(m_{\alpha\gamma} - \frac{1}{R_{\alpha\gamma}}\right) + \kappa_{\beta\gamma}\left(m_{\beta\gamma} - \frac{1}{R_{\beta\gamma}}\right)\right] \tag{S19}$$

for an exocytic contact line neck adjacent to an out-budded two-droplet vesicle with positive mean curvatures $M_{\alpha\gamma} = +1/R_{\alpha\gamma}$ and $M_{\beta\gamma} = +1/R_{\beta\gamma}$ as in Fig. 5b.

On the other hand, for an endocytic contact line neck adjacent to an in-budded two-droplet vesicle with $R_{\alpha\gamma} > R_{\beta\gamma}$, positive mean curvature $M_{\alpha\gamma} = +1/R_{\alpha\gamma}$, and negative mean curvature $M_{\beta\gamma} = -1/R_{\beta\gamma}$ as in Fig. 5a, the coefficient ζ_{be} in eqn (S18) is equal to

$$\zeta_{\mathrm{be}} = \zeta_{\mathrm{be}}^{\mathrm{end}} \equiv 4\pi \left[\kappa_{\alpha\gamma}(M_{\alpha\gamma} - m_{\alpha\gamma}) + \kappa_{\beta\gamma}(M_{\beta\gamma} - m_{\beta\gamma})\right] = 4\pi \left[\kappa_{\alpha\gamma}\left(\frac{1}{R_{\alpha\gamma}} - m_{\alpha\gamma}\right) + \kappa_{\beta\gamma}\left(-\frac{1}{R_{\beta\gamma}} - m_{\beta\gamma}\right)\right]. \tag{S20}$$

In addition to the contribution from the bending energy, the circular contact line with radius R_{cl} and line tension λ_{cl} contributes the free energy

$$E_{\mathrm{cl}}(R_{\mathrm{ne}}) = 2\pi R_{\mathrm{cl}} \lambda_{\mathrm{cl}} = 2\pi R_{\mathrm{ne}} \lambda_{\mathrm{cl}} \tag{S21}$$

where the second equality follows from $R_{\mathrm{cl}} = R_{\mathrm{ne}}$.

The total energy E_{2Dr} of the two-droplet vesicle with a closing contact line neck is then given by the asymptotic equality

$$E_{\mathrm{2Dr}} \approx E_{\mathrm{2Sph}} + \zeta_{\mathrm{be}} R_{\mathrm{ne}} + 2\pi\lambda_{\mathrm{cl}} R_{\mathrm{ne}} \quad \text{for small neck radius } R_{\mathrm{ne}} = R_{\mathrm{cl}}, \tag{S22}$$

up to first order in R_{ne} which implies the constriction force

$$f \equiv \left.\frac{\partial E_{\mathrm{2Dr}}}{\partial R_{\mathrm{ne}}}\right|_{R_{\mathrm{ne}}=0} = \zeta_{\mathrm{be}} + 2\pi\lambda_{\mathrm{cl}} \tag{S23}$$

with $\zeta_{\mathrm{be}} = \zeta_{\mathrm{be}}^{\mathrm{exo}}$ for an exocytic contact line neck as in Eq (S19) and $\zeta_{\mathrm{be}} = \zeta_{\mathrm{be}}^{\mathrm{end}}$ for an endocytic contact line neck with $R_{\alpha\gamma} > R_{\beta\gamma}$ as in Eq (S20). Thus, the constriction force at a closed contact line neck has the form

$$f = f^{\mathrm{exo}} \equiv 4\pi \left[\kappa_{\alpha\gamma}\left(m_{\alpha\gamma} - \frac{1}{R_{\alpha\gamma}}\right) + \kappa_{\beta\gamma}\left(m_{\beta\gamma} - \frac{1}{R_{\beta\gamma}}\right)\right] + 2\pi\lambda_{\mathrm{cl}} \quad \text{for an exocytic contact line neck} \tag{S24}$$

and

$$f = f^{\mathrm{end}} \equiv 4\pi \left[\kappa_{\alpha\gamma}\left(\frac{1}{R_{\alpha\gamma}} - m_{\alpha\gamma}\right) + \kappa_{\beta\gamma}\left(-\frac{1}{R_{\alpha\gamma}} - m_{\alpha\gamma}\right)\right] + 2\pi\lambda_{\mathrm{cl}} \quad \text{for an endocytic contact line neck} \tag{S25}$$

with $R_{\alpha\gamma} > R_{\beta\gamma}$.

S8.7 Total energy of two-droplet vesicle during the closure of a contact line neck

During the closure of an open membrane neck, the $\alpha\beta$ interface forms a spherical cap across this neck, which meets the membrane along a circular contact line with radius $R_{\rm cl}$ as depicted in Fig. 14 of the main text. The area $A_{\alpha\beta}$ of this $\alpha\beta$ interface contributes the term[25]

$$E_{\alpha\beta} \equiv \Sigma_{\alpha\beta} A_{\alpha\beta} = \frac{2\pi}{1+\sin\theta_\alpha^*} \Sigma_{\alpha\beta} R_{\rm cl}^2 \,, \tag{S26}$$

to the free energy of the vesicle-droplet system, where θ_α^* represents the intrinsic contact angle of the condensate droplet at the membrane, see Fig. 14 and Section 11.3 of the main text. For a contact line neck with $R_{\rm cl} = R_{\rm ne}$, the interfacial free energy $E_{\alpha\beta}$ is proportional to $R_{\rm cl}^2 = R_{\rm ne}^2$, which implies that $E_{\alpha\beta}$ represents a second-order term for the energy $E_{\rm 2Dr}(R_{\rm ne})$ compared to the first-order expression in eqn (S22). A combination of eqn (S22) and eqn (S26) with $R_{\rm cl} = R_{\rm ne}$ then leads to the total energy

$$E_{\rm 2Dr}(R_{\rm ne}) \approx E_{\rm 2Sph} + f R_{\rm ne} + c_{\alpha\beta} \Sigma_{\alpha\beta} R_{\rm ne}^2 \quad \text{for small } R_{\rm ne} = R_{\rm cl} \text{ with} \quad c_{\alpha\beta} \equiv \frac{2\pi}{1+\sin\theta_\alpha^*} \tag{S27}$$

up to second order in the radius $R_{\rm ne}$ of the closing contact line neck, which is equivalent to eqn (12) and (13) of the main text.

S9 Affinity contrast between coexisting aqueous phases at membranes

Adhesion free energy and affinity contrast. As shown in ref. 25, the shape functional for vesicle-droplet systems contains the term ΣA, which depends on the mechanical membrane tension Σ, which is conjugate to the total membrane area A, and on the adhesion free energy

$$E_{\rm ad} = W_{\alpha\gamma} A_{\alpha\gamma} + W_{\beta\gamma} A_{\beta\gamma} = W_{\alpha\gamma} A + (W_{\beta\gamma} - W_{\alpha\gamma}) A_{\beta\gamma} \,. \tag{S28}$$

which involves the the adhesive strength, $W_{\alpha\gamma}$ and $W_{\beta\gamma}$, of the two aqueous phases, where the adhesive strengths are equal to the adhesion free energies per unit area. When we combine these two terms, we obtain[25]

$$\Sigma A + E_{\rm ad} = \Sigma^{\rm m}_{\alpha\gamma} A_{\alpha\gamma} + \Sigma^{\rm m}_{\beta\gamma} A_{\beta\gamma} \tag{S29}$$

with the mechanical tensions

$$\Sigma^{\rm m}_{\alpha\gamma} \equiv \Sigma + W_{\alpha\gamma} \quad \text{and} \quad \Sigma^{\rm m}_{\beta\gamma} \equiv \Sigma + W_{\beta\gamma} \,. \tag{S30}$$

of the $\alpha\gamma$ and $\beta\gamma$ membrane segments. Thus, each segment tension $\Sigma_{j\gamma}$ with $j = \alpha$ of β depends both on the mechanical membrane tension Σ and on the adhesive strengths $W_{j\gamma}$.

For a given batch of GUVs, the mechanical tension Σ depends on the vesicle size and shape, which implies that Σ varies from vesicle to vesicle.[26] In contrast, the adhesive strength $W_{j\gamma}$ is determined by the molecular interactions across the leaflet-water interfaces and should have the same value for all GUVs from the same batch, assuming that their membranes have the same molecular composition and are exposed to aqueous solutions with the same solute composition. As a consequence, the difference

$$\Sigma^{\rm m}_{\beta\gamma} - \Sigma^{\rm m}_{\alpha\gamma} = W_{\beta\gamma} - W_{\alpha\gamma} \equiv W_{\beta\alpha} \tag{S31}$$

of the two segment tensions is equal to the difference of the two adhesive strengths $W_{\beta\gamma}$ and $W_{\alpha\gamma}$, which defines the affinity contrast $W_{\beta\alpha}$ as in eqn (21).

Affinity contrast and force balance. The difference $\Sigma^{\rm m}_{\beta\gamma} - \Sigma^{\rm m}_{\alpha\gamma}$ of the two segment tensions also satisfies the force balance equation $\Sigma^{\rm m}_{\beta\gamma} - \Sigma^{\rm m}_{\alpha\gamma} = \Sigma_{\alpha\beta} \cos\theta_\alpha^*$ as in eqn (16), which follows directly from the requirement that the two membrane segments have a common tangent plane at the contact line, as depicted in Fig. 16. For an axisymmetric shape parametrized by the arc length s and the tilt angle $\psi = \psi(s)$ of the membrane's normal

vector[27–29], this requirement implies that the tilt angle $\psi(s)$ is continuous at the contact line. In contrast, the first derivative $\mathrm{d}\psi/\mathrm{d}s$ of the tilt angle is discontinuous at the contact line when the two membrane segments $\alpha\gamma$ and $\beta\gamma$ have different curvature-elastic properties.[25]

The discontinuity of $\mathrm{d}\psi/\mathrm{d}s$ at the contact line leads to additional correction terms for the force balance relation in eqn (16). These correction terms depend both on the curvature-elastic parameters of the two membrane segment and on the principal curvatures of these membrane segments on the two sides of the contact line.[25,28] As a consequence, these correction terms are difficult to estimate in general and have been ignored in eqn (16). When we combine eqn (16) with eqn (S31), we obtain

$$\Sigma^{\mathrm{m}}_{\beta\gamma} - \Sigma^{\mathrm{m}}_{\alpha\gamma} = \Sigma_{\alpha\beta}\cos\theta^*_\alpha = W_{\beta\alpha}\,, \tag{S32}$$

which represents a relationship between the interfacial tension $\Sigma_{\alpha\beta}$, the intrinsic contact angle θ^*_α, and the affinity contrast $W_{\beta\alpha}$. The interfacial tension $\Sigma_{\alpha\beta}$ is a material parameter, which is independent of the size and shape of the individual condensate droplets. The relationship in eqn (S32) then implies that both the intrinsic contact angle θ^*_α and the affinity contrast $W_{\alpha\beta}$ represent material parameters as well. Therefore, when we ignore the additional correction terms for the force balance relation in eqn (16), we conclude from eqn (S32) that vesicle-droplet systems involve three material parameters as given by $\Sigma_{\alpha\beta}$, θ^*_α, and $W_{\beta\alpha}$. It remains to be seen, however, whether or not this conclusion is affected by the additional correction terms for the force balance relation.

S10 Measured values of intrinsic contact angles

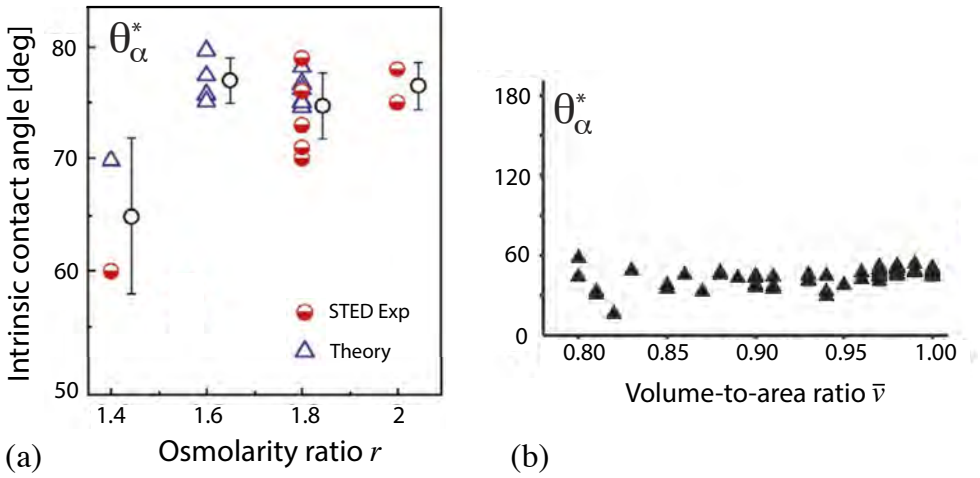

Figure S11 Experimental values for the intrinsic contact angle θ^*_α as determined by two different methods: (a) Intrinsic contact angle θ^*_α (red circles) as measured by STED microscopy for different osmolarity ratios r.[44] The parameter r represents the ratio of exterior osmolarity to initial interior osmolarity, which increases during the osmotic deflation of the vesicle. For comparison, the black triangles represent the theoretical values as calculated via eqn (27) from the apparent contact angles θ_α, θ_β, and θ_γ, which were determined by independent measurements; and (b) Intrinsic contact angle θ^*_α for 63 individual vesicles with different values of the volume-to-area ratio $\bar{v}$. These θ^*_α-values were obtained from eqn (27) and the apparent contact angles displayed in Fig. 18.[29]. As a result, one obtains the estimates $\cos\theta^*_\alpha = 0.714 \pm 0.075$ and $\theta^*_\alpha \simeq 44.4^\circ$

References

[1] P. A. Albertsson, *Partition of Cell Particles and Macromolecules: Separation and Purification of Biomolecules, Cell Organelles Membranes, and Cells in Aqueous Polymer Two-Phase Systems and Their Use in Biochemical Analysis and Biotechnology*, Wiley, 3rd edn, 1986.

[2] J. Esquena, *Curr. Opin. Colloid Interface Sci.*, 2016, **25**, 109–119.

[3] Y. Liu, R. Lipowsky and R. Dimova, *Langmuir*, 2012, **28**, 3831–3839.

[4] R. Ghosh, V. Satarifard, A. Grafmüller and R. Lipowsky, *ACS Nano*, 2021, **15**, 7237–7248.

[5] A. W. Fritsch, A. F. Diaz-Delgadillob, O. Adame-Arana, C. Hoege, M. Mittasch, M. Kreysing, M. Leaver, A. A. Hyman, F. Jülicher and C. A. Weber, *PNAS*, 2021, **118**, e2102772118.

[6] J. W. Cahn and J. E. Hilliard, *J. Chem. Phys.*, 1958, **28**, 258–267.

[7] B. Widom, *J. Chem. Phys.*, 1965, **43**, 3892–3897.

[8] R. Lipowsky, *Faraday Discuss.*, 2013, **161**, 305–331.

[9] R. Lipowsky, *Physics of Biological Membranes*, Springer, 2018, pp. 1–44.

[10] D. Cuvelier, I. Derenyi, P. Bassereau and P. Nassoy, *Biophys. J.*, 2005, **88**, 2714 – 2726.

[11] B. Sorre, A. Callan-Jones, J. Manzi, B. Goud, J. Prost, P. Bassereau and A. Roux, *PNAS*, 2012, **109**, 173 – 178.

[12] M. Karimi, J. Steinkühler, D. Roy, R. Dasgupta, R. Lipowsky and R. Dimova, *Nano Lett.*, 2018, **18**, 7816–7821.

[13] D. Roy, J. Steinkühler, Z. Zhao, R. Lipowsky and R. Dimova, *Nano Lett.*, 2020, **20**, 3185–3191.

[14] C. Delaunay, *J. Math. Pures et Appl. Sér. 1*, 1841, **6**, 309–320.

[15] R. Lipowsky, *Adv. Colloid Interface Sci.*, 2022, **301**, 102613.

[16] R. Lipowsky, S. Pramanik, A. S. Benk, M. Tarnawski, J. P. Spatz and R. Dimova, *ACS Nano*, 2023, **17**, 11957–11968.

[17] Y. Liu, J. Agudo-Canalejo, A. Grafmüller, R. Dimova and R. Lipowsky, *ACS Nano*, 2016, **10**, 463–474.

[18] T. Bhatia, S. Christ, J. Steinkühler, R. Dimova and R. Lipowsky, *Soft Matter*, 2020, **16**, 1246–1258.

[19] J. Steinkühler, R. L. Knorr, Z. Zhao, T. Bhatia, S. Bartelt, S. Wegner, R. Dimova and R. Lipowsky, *Nature Commun.*, 2020, **11**, 905.

[20] M. Heinrich, A. Tian, C. Esposito and T. Baumgart, *Proc. Nat. Acad. Sci. USA*, 2010, **107**, 7208 – 7213.

[21] J. Henriksen, A. C. Rowat and J. H. Ipsen, *Eur. Biophys. J.*, 2004, **33**, 732–741.

[22] L. R. Arriaga, I. Lopez-Montero, F. Monroy, G. Orts-Gil, B. Farago and T. Hellweg, *Biophys. J.*, 2009, **96**, 3629–3637.

[23] R. Dimova, *Adv. Colloid Interface Sci.*, 2014, **208**, 225–234.

[24] M. A. S. Karal, M. B. ad M. Ahmed and K. Ahamed, *Soft Matter*, 2023, **19**, 8285–8304.

[25] R. Lipowsky, *J. Phys. Chem. B*, 2018, **122**, 3572–3586.

[26] R. Lipowsky, *Adv. Biology*, 2022, **6**, 2101020.

[27] U. Seifert, K. Berndl and R. Lipowsky, *Phys. Rev. A*, 1991, **44**, 1182–1202.

[28] F. Jülicher and R. Lipowsky, *Phys. Rev. E*, 1996, **53**, 2670–2683.

[29] H. Kusumaatmaja, Y. Li, R. Dimova and R. Lipowsky, *Phys. Rev. Lett.*, 2009, **103**, 238103.

[30] *The Scientific Papers of J. Willard Gibbs*, Longman, Green, and Co., 1906, vol. I.

[31] J. Rowlinson and B. Widom, *Molecular Theory of Capillarity*, Oxford University Press, Oxford, 1989.

[32] J. K. Berg, C. M. Weber and H. Riegler, *Phys. Rev. Lett.*, 2010, **105**, 076103.

[33] H. Matsubara, B. Ushijima, B. M. Law, T. Takiue and M. Aratono, *Adv. Colloid Interfac.*, 2014, **206**, 186 – 194.

[34] J. H. Weijs, A. Marchand, B. Andreotti, D. Lohse and J. H. Snoeijer, *Phys. Fluids*, 2011, **23**, 022001.

[35] J.-C. Geminard, A. Zywocinski, F. Caillier and P. Oswald, *Phil. Mag. Let.*, 2004, **84**, 199 – 204.

[36] B. Różycki and R. Lipowsky, *J. Chem. Phys.*, 2015, **142**, 054101.

[37] A. Sreekumari and R. Lipowsky, *J. Chem. Phys.*, 2018, **149**, 084901.

[38] R. Ghosh, V. Satarifard, A. Grafmüller and R. Lipowsky, *Nano Lett.*, 2019, **19**, 7703–7711.

[39] R. Ghosh, V. Satarifard and R. Lipowsky, *Nature Commun.*, 2023, **14**, 615.

[40] R. Lipowsky, R. Ghosh, V. Satarifard, A. Sreekumari, M. Zamaletdinov, B. Różycki, M. Miettinen and A. Grafmüller, *Biomolecules*, 2023, **13**, 926.

[41] R. Lipowsky, *Multiresponsive Behavior of Biomembranes and Giant Vesicles*, Elsevier, London, UK, 2019, vol. 30, ch. 3, pp. 105–155.

[42] R. Lipowsky, *Membranes*, 2023, **13**, 223.

[43] A. Mangiarotti, M. Aleksanyan, M. Siri, T.-W. Sun, R. Lipowsky and R. Dimova, *Adv. Sci.*, 2024, **11**, 2309864.

[44] Z. Zhao, D. Roy, J. Steinkühler, T. Robinson, R. Lipowsky and R. Dimova, *Adv. Materials*, 2022, **34**, 2106633.